IDRLP: Image Dehazing Using Region Line Prior

Mingye Ju, Can Ding, *Member, IEEE,* Charles A. Guo, Wenqi Ren, *Member, IEEE,* and Dacheng Tao, *Fellow, IEEE*

***Abstract*—In this work, a novel and ultra-robust single image dehazing method called IDRLP is proposed. It is observed that when an image is divided into n regions, with each region having a similar scene depth, the brightness of both the hazy image and its haze-free correspondence are positively related with the scene depth. Based on this observation, this work determines that the hazy input and its haze-free correspondence exhibit a quasi-linear relationship after performing this region segmentation, which is named as region line prior (RLP). By combining RLP and the atmospheric scattering model (ASM), a recovery formula (RF) can be easily obtained with only two unknown parameters, i.e., the slope of the linear function and the atmospheric light. A 2-D joint optimization function considering two constraints is then designed to seek the solution of RF. Unlike other comparable works, this "joint optimization" strategy makes efficient use of the information across the entire image, leading to more accurate results with ultra-high robustness. Finally, a guided filter is introduced in RF to eliminate the adverse interference caused by the region segmentation. The proposed RLP and IDRLP are evaluated from various perspectives and compared with related state-of-the-art techniques. Extensive analysis verifies the superiority of IDRLP over state-of-the-art image dehazing techniques in terms of both the recovery quality and efficiency. A software release is available at https://sites.google.com/site/renwenqi888/.**

***Index Terms*—Atmospheric scattering model, image dehazing, region segmentation, 2-D joint optimization.**

I. Introduction

UNDER hazy weather, due to interference from particles suspended in the atmosphere, images taken by cameras commonly lose important features, e.g., edge visibility and color quality. This image degradation not only negatively impacts the subjective user experience but also impedes the subsequent processing of such images by intelligent systems that require high-quality inputs. Thus image dehazing has been investigated in this paper for the purpose of restoring these blurred textures and excluding such visual interferences from hazy images.

This work was supported by National Natural Science Foundation of China (61902198), Natural Science Foundation of Jiangsu Province (BK20190730), Research Foundation of Nanjing University of Posts and Telecommunications (NY219135), and in part by Key Laboratory of Radar Imaging and Microwave Photonics, Ministry of Education, for Nanjing University of Aeronautics and Astronautics.

M. Ju is with the School of Internet of Things, Nanjing University of Posts and Telecommunications, Nanjing, 210000, China. e-mail:(Jumingye@njupt.edu.cn)

C. Ding is with the Global Big Data Technologies Centre (GBDTC), University of Technology Sydney (UTS), Ultimo, NSW, 2007, Australia. e-mail:(Can.Ding@uts.edu.au)

C. A. Guo and D. Tao are with the School of Computer Science,the University of Sydney, Camperdown, NSW, 2006, Australia. e-mail:(dacheng.tao@sydney.edu.au)

W. Ren is with the State Key Laboratory of Information Security, Institute of Information Engineering, Chinese Academy of Sciences, Beijing, 100000, China. e-mail:(renwenqi@iie.ac.cn)

The current state-of-the-art dehazing algorithms can be roughly divided into two categories: image-enhancing methods and atmospheric scattering model (ASM)-based techniques. The former class of algorithms simply employ traditional image processing methods [1]–[6] to enhance the contrast of hazy images. Although local or global contrast can be improved, the visual quality of recovered results is very limited because the precise characteristics of image haze theory are not considered. To achieve a better restoration, Refs. [7]–[11] have devised some fusion approaches that can preprocess an input image using two or more traditional methods and then blend the useful information contained in the preprocessed images. Although these fusion approaches display improved recovery quality, their performance is still largely dependent on the effectiveness of the preprocessing methods. In comparison, the ASM-based techniques exhibit a more competitive restoration capability [12]. Mathematically, ASM is expressed as follows:

$$\boldsymbol{I}(x,y) = \boldsymbol{A} \cdot \boldsymbol{\rho}(x,y) \cdot t(x,y) + \boldsymbol{A} \cdot (1 - t(x,y)), \quad (1)$$

where $\boldsymbol{I}$ is the hazy image, $\boldsymbol{A}$ is the atmospheric light, t is the medium transmission, and $\boldsymbol{\rho}$ is the scene albedo or haze-free result. The success of ASM-based dehazing methods lies in either inferring the latent priors or relying on intensive data-processing to model the transmission and estimate the atmospheric light, and then theoretically eliminating the haze cover in an image via ASM. Depending on the manner of characterising this transmission, ASM-based dehazing methods can be further divided into pixel-wise, patch-wise, learning-wise, and non-local-wise strategies.

Pixel-wise strategy: As illustrated in Fig. 1(a), the basic idea of this strategy is to utilize the minimum color value of each pixel to construct the transmission estimation formula [13]–[16]. Its main advantage is its low complexity as well as its relatively short processing time. However, the minimum channel contains lots of improper textures [17], [18], which necessitates the use of an additional control factor and subsequent blur operators to remedy this drawback. For example, by assuming a quadratic relationship between hazy images and their corresponding haze-free counterparts, Wang et al. [13] derived a simple formula for estimating transmissions, and then used Gaussian filter to remove improper details in the rough transmission. Although pixel-wise-strategy-based algorithms can produce realistic results for the majority of test cases, having to manually regulate the control factor limits their applicability.

Patch-wise strategy: The patch-wise strategy illustrated in Fig. 1(b) determines the transmission map by extracting local information from each patch rather than from each pixel. Since a patch contains richer information than a single pixel, the patch-wise strategy [19]–[25] features a stronger restoration

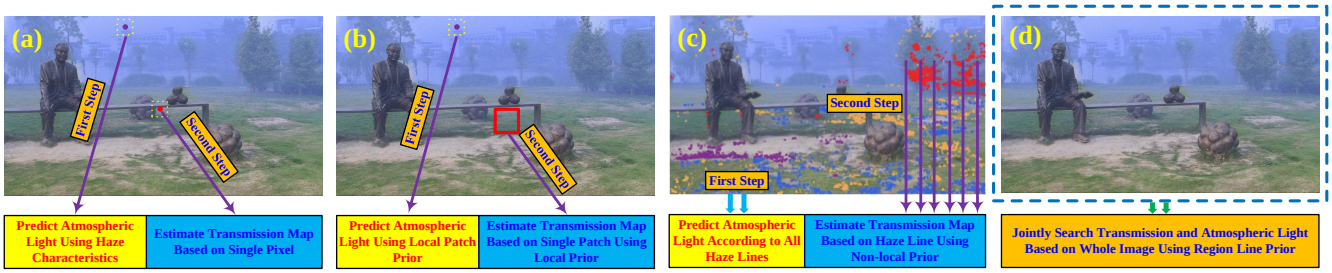

Fig. 1. Working mechanisms of different ASM-based image dehazing strategies. **(a)**: Pixel-wise strategy. **(b)**: Patch-wise strategy. **(c)**: Non-local-wise strategy. **(d)**: Joint optimization strategy.

ability compared to the pixel-wise strategy. On the other hand, it is necessary to deploy time-consuming guided tools, e.g., soft matting and bilateral filter, to exclude the block artifacts resulting from this strategy. The most representative patch-wise-strategy-based technique is the dark channel prior (DCP) method [19], which can directly detect the haze distribution from a hazy image and obtain a haze-free output by employing soft matting to refine the rough transmission. The limitation of DCP is that this technique may result in over-enhancement when dealing with the scenes where the brightness of objects is similar to that of the atmospheric light. To attain more information for transmission estimation, another similar strategy was advocated in [26], [27] in which the central idea is to expand the transmission estimation range from patch to scene, thus enabling the restoration performance to be improved to some extent.

Learning-wise Strategy: Benefiting from the rapid development of machine learning, ASM-based haze removal can also be realized by adopting a learning-wise strategy [28]–[38]. For example, inspired by multiple conventional priors, a convolutional neural network (CNN) based network called DehazeNet was put forward in [28] to estimate the transmission map using an end-to-end manner. In [29], a unsupervised training deep neural network was proposed by Golts et al. This method designed a DCP loss function to overcome the shortcomings of synthetic data and solely used real-world images to tune the network's parameters. To reduce the accumulation of errors during estimating imaging parameters, Ref. [33] remodeled transmission and atmospheric light to be a new variable and then used a light-weight network to achieve an end-to-end haze removal. The main advantage of this strategy is that it can blindly and autonomously merge or train the multiple haze-relevant features to get an accurate transmission map, but usually a large number of samples are required for training purpose. Here we remark that there is another mechanism [39]–[46] for learning-wise-based image haze removal, which does not rely on ASM but directly learns the potential transposition between hazy image and scene albedo. Such mechanism does not need to estimate transmission and atmospheric light. Typically, Li et al. [46] developed a perception-inspired image enhancement system composed of haze removal subnetwork and refinement subnetwork. However, its reliance on machine learning makes the dehazing process to function as a black box and thus less domain knowledge is involved in the learning procedure, which may result in degradation of the recovery performance.

Non-local-wise Strategy: Unlike the three local strategies discussed before, the non-local-wise strategy is based on a key observation that a hazy image usually contains clusters of similar colors in RGB space [47], [48] as well as recurrence of small image patches [**?**], which enables us to calculate the transmission set of these attributes distributed over the entire image plane. Taking the color lines method [47] shown in Fig. 1(c) as an example, the prerequisite to using this method is to recognize the haze-lines in an input image, i.e., the coordinate set of distinct colors. According to these color lines, the atmospheric light and transmission map are then estimated by using a non-local prior. Relying on these estimated parameters, the haze cover in an image can be finally removed via ASM. Despite the fact that very reliable results can be obtained for most situations, this method may fail to handle scenes with heavy haze since the accuracy of color classification may decrease as the haze level increases.

In addition to the aforementioned deficiencies, there is a disadvantage that is common to all of these non-learning-wise ASM-based dehazing techniques, i.e., ignoring the latent connection between imaging parameters. As evident in Figs. 1(a), 1(b), and 1(c), the pixel-wise, patch-wise, and non-local-wise strategies all follow the same routine, i.e., Predict atmospheric light $\rightarrow$ Estimate transmission map $\rightarrow$ Scene recovery. Once one fails to accurately predict the atmospheric light, which is well within the realm of possibility, the subsequent transmission map estimation is bound to be disturbed. This leads to a fact that although existing non-learning-wise ASM-based image dehazing techinqiues all exhibit some advantages, none of them have been shown to handle all practical situations, i.e., indicating a relatively low robustness.

In this paper, an extremely robust prior knowledge, i.e., region line prior (RLP), is proposed. RLP is based on an image statistic that the average pixel intensities of different regions distributed over the hazy image plane has a quasi-linear relationship with those over the corresponding haze-free image. Based on RLP and ASM, a fast image dehazing technique (IDRLP) employing a joint optimization strategy is developed. The proposed IDRLP converts the highly ill-posed image dehazing task into a simple 2-D joint optimization function (2D-JOF), which significantly shrinks the solution space of haze removal. Moreover, this novel joint optimization strategy makes use of the information across the entire image rather than that from a single pixel (pixel-wise strategy), a local patch

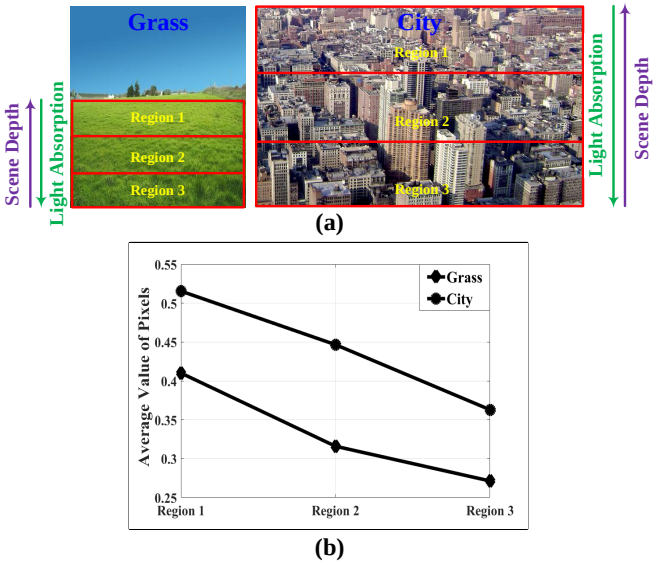

Fig. 2. Two examples to illustrate the observation that a farther region corresponds to a greater average brightness in haze-free images.

(patch-wise strategy), or non-local objects (non-local wise strategy) to estimate the imaging parameters, as illustrated in Fig. 1(d), which leads to more reliable restoration. Without the need for introducing any extra operations, IDRLP is able to remove the haze cover from various kinds of challenging hazy images while avoiding several common drawbacks in the dehazed results, e.g., over-enhancement, over-saturation, and mist residue.

II. Region Line Prior (RLP)

It is commonly known that ASM-based image haze removal is a highly ill-posed problem due to the absence of information describing the atmospheric light and the medium transmission, both of which affect the degree of interference due to haze. In this section, a novel prior, i.e., RLP, is proposed to expand the information that can be inferred from a hazy image relating to its scene albedo. It is based on an observation that farther scenes usually appear to be brighter than nearer scenes for both hazy and haze-free images.

Fig. 2 illustrates two examples of haze-free images, i.e., a field of grass and a city. Three regions with similar texture but different scene depths are selected and their average value of pixels are calculated. It is found that the farther regions with greater scene depth have a higher average value of pixels. In ideal case, by assuming all scene objects have Lambertian surfaces, the brightness is actually not related to scene depth. The derivation of the ideal case can be found in our supplementary material. However, in reality, Lambertian surface does not exist. It was demonstrated in [49] that huge deviations from the Lambert law are ubiquitous. This is mainly because most surfaces have rough textures in which lights get diffracted, scattered, and trapped. This light absorption phenomenon is observed in both micro and macro level and it will reduce the brightness of objects captured by camera [25], [50]. In general, the smaller the scene depth, the higher the intensity of the textures observed from camera, the stronger the light absorption effect, thus the lower the average brightness. When taking consideration of the light absorption rate varying with different scene depth, the conclusion agrees with the observation. Considering an image that can be divided into n regions with each region having a similar scene depth, there exists a relationship between the scene albedo and the scene depth:

$$\begin{aligned}\hat{\rho}_m &= \tfrac{1}{3\cdot|\Omega_m|}\sum_{(x,y)\in\Omega_m}\sum_{\mathrm{c}\in\{\mathrm{R,G,B}\}}\rho^{\mathrm{c}}(x,y)\\ &\propto \hat{d}_m = \tfrac{1}{|\Omega_m|}\sum_{(x,y)\in\Omega_m} d(x,y),\end{aligned} \tag{2}$$

where $m \in \{0, n-1\}$, $\mathrm{c} \in \{\mathrm{R,G,B}\}$ is the color index, d is the scene depth, Ω_m is the coordinate set of pixels in the m^{th} region, and $|\Omega_m|$ represents the number of pixels in Ω_m.

It is commonly known that for hazy images, the average value of pixels in each region also increases with the scene depth [51] as a result of haze interference, thus we have

$$\hat{I}_m = \frac{1}{3\cdot|\Omega_m|}\sum_{(x,y)\in\Omega_m}\sum_{\mathrm{c}\in\{\mathrm{R,G,B}\}} I^{\mathrm{c}}(x,y) \propto \hat{d}_m. \tag{3}$$

Statistical results of a large number of images confirm the validity of above conclusions that the average brightness generally increases with the scene depth for both hazy and haze-free images. Fig. 3 shows a statistical analysis of eight examples collected from the SOTS dataset [52], where each sample is composed of a hazy image and a haze-free ground truth correspondence. In this experiment, we first manually located the atmospheric light for the hazy image in each sample, and then calculated the depth map via ASM using the recorded atmospheric light and the sample data. Note that the scattering coefficient here is initialized to be one. Next, the obtained depth maps were blurred by guided filter [53] and divided into n (n = 10 in this case) regions with similar depth by K-means [54]. Subsequently, the values of $\hat{d}$, $\hat{\rho}$, and $\hat{I}$ for each region were calculated via Eqs. (2) and (3). According to Fig. 3, it is clear that both $\hat{I}_m$ and $\hat{\rho}_m$ are positively related with $\hat{d}_m$ and their curves on each sample appear to be very similar, which raises the question of whether $\hat{I}_m$ and $\hat{\rho}_m$ can be directly correlated as well.

To determine the answer, we further illustrate the statistical results of $\hat{I}_m$ and $\hat{\rho}_m$ on twelve sample images in Fig. 4. It can be concluded from this figure that $\hat{I}$ and $\hat{\rho}$ do exhibit a quasi-linear relationship for all the given examples. Moreover, for each image, the $\hat{\rho}$ value for the region with the minimum scene depth is always close to 0.1. Based on this observation, the correlation between $\hat{\rho}$ and $\hat{I}$ is determined to be a linear function, named as region line prior (RLP):

$$\hat{\rho}_m \cong k\cdot\left(\hat{I}_m - \hat{I}_0\right) + 0.1, \tag{4}$$

where k represents the slope and $\hat{I}_0$ is the $\hat{I}$ value of the region with the minimum scene depth. Different from the existing image priors, RLP is a non-local-wise region-based strategy relying on the intrinsic relationship between the hazy image and the scene albedo, which facilitates the subsequent haze removal process.

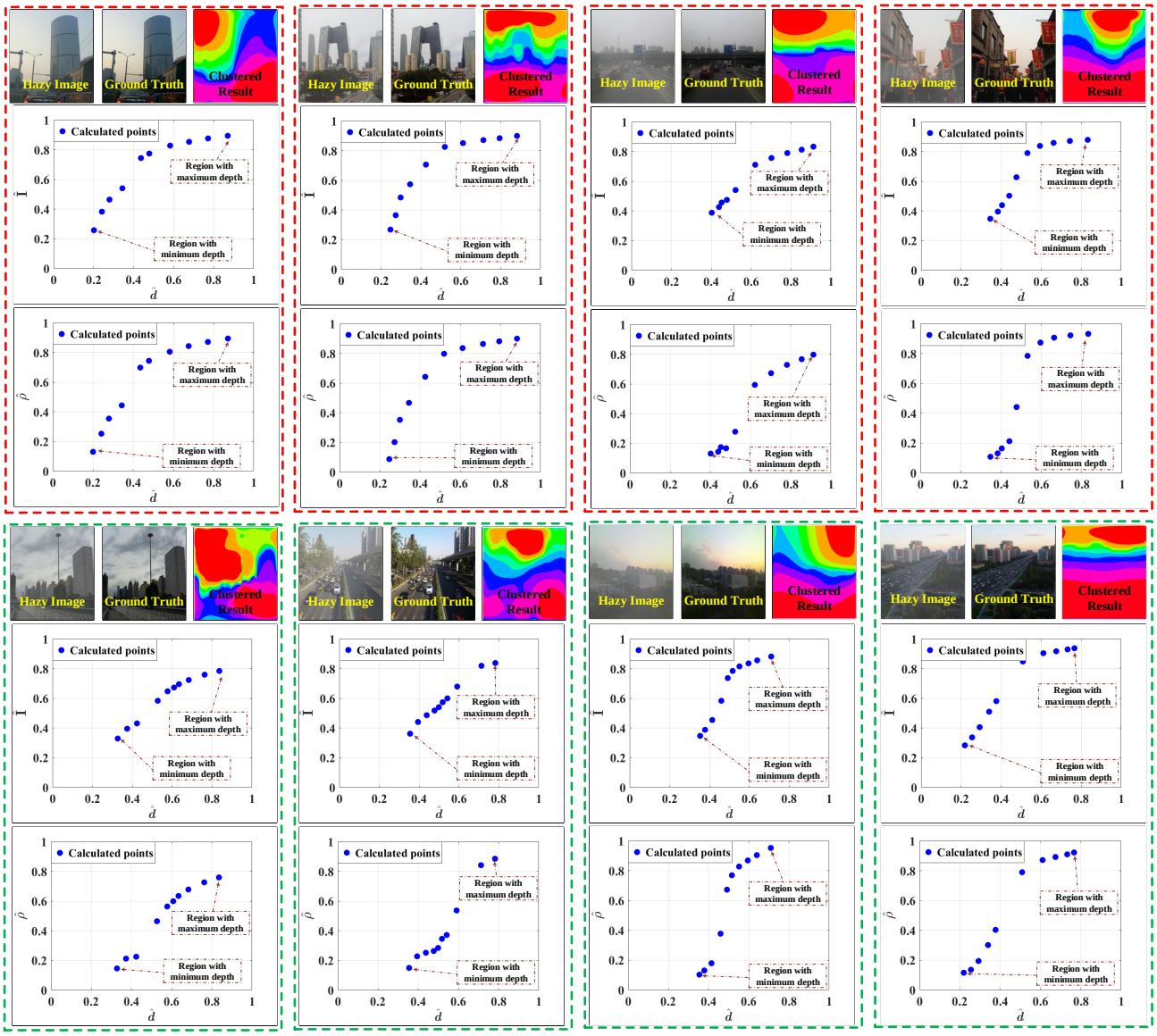

Fig. 3. Statistical results to confirm that the average brightness increases with the scene depth for both hazy and haze-free images.

III. Image Dehazing Based on RLP (IDRLP)

In this section, based on the proposed RLP and ASM, a simple yet effective image dehazing technique, i.e., IDRLP, is developed. Three modules are utilized in IDRLP: an a priori constraint to deduce the recovery formula (RF), a joint optimization module used to search the optimal slope and the atmospheric light in the RF, and a scene restoration module.

A. A Priori Constraint

The first step of IDRLP is to divide the hazy image into n non-overlapping regions with each region having a similar depth. However, since explicit depth information is unavailable, it is difficult to carry out region segmentation (RS) directly on a depth map. Therefore, we employ K-means [54] here to execute the RS on the blue channel of hazy image I^b since its distribution is very similar to the scene depth [55]–[57]. After the RS, each region is assumed to have the same transmission value. For example, in the m^{th} region where $(x, y) \in \Omega_m$, the transmission $t(x, y) \approx \hat{t}_m$. In this case, ASM can be applied to any defined region and simplified as

$$\boldsymbol{I}(x, y) = \boldsymbol{A} \cdot \boldsymbol{\rho}(x, y) \cdot \hat{t}_m + \boldsymbol{A} \cdot \left(1 - \hat{t}_m\right), \tag{5}$$

where $(x, y) \in \Omega_m$ and $m \in \{0, n-1\}$. Taking the mean for the m^{th} region on both sides of Eq. (5) yields

$$\hat{I}_m = \bar{A} \cdot \hat{\rho}_m \cdot \hat{t}_m + \bar{A} \cdot \left(1 - \hat{t}_m\right), \tag{6}$$

where $\bar{A}$ is the mean of $\boldsymbol{A}$. Combining Eqs. (4) and (6), the transmission of the m^{th} region can be obtained as

$$\hat{t}_m = \frac{\hat{I}_m - \bar{A}}{\bar{A} \cdot \left(k \cdot \left(\hat{I}_m - \hat{I}_0\right) - 0.9\right)}. \tag{7}$$

Substituting Eq. (7) into Eq. (5), the recovery formula (RF) for the m^{th} region used for haze removal can be derived as

$$\boldsymbol{\rho}(x, y) = 1 - \frac{\bar{A} \cdot \left(k \cdot \left(\hat{I}_m - \hat{I}_0\right) - 0.9\right)}{\hat{I}_m - \bar{A}} \cdot \frac{\boldsymbol{A} - \boldsymbol{I}(x, y)}{\boldsymbol{A}}, \tag{8}$$

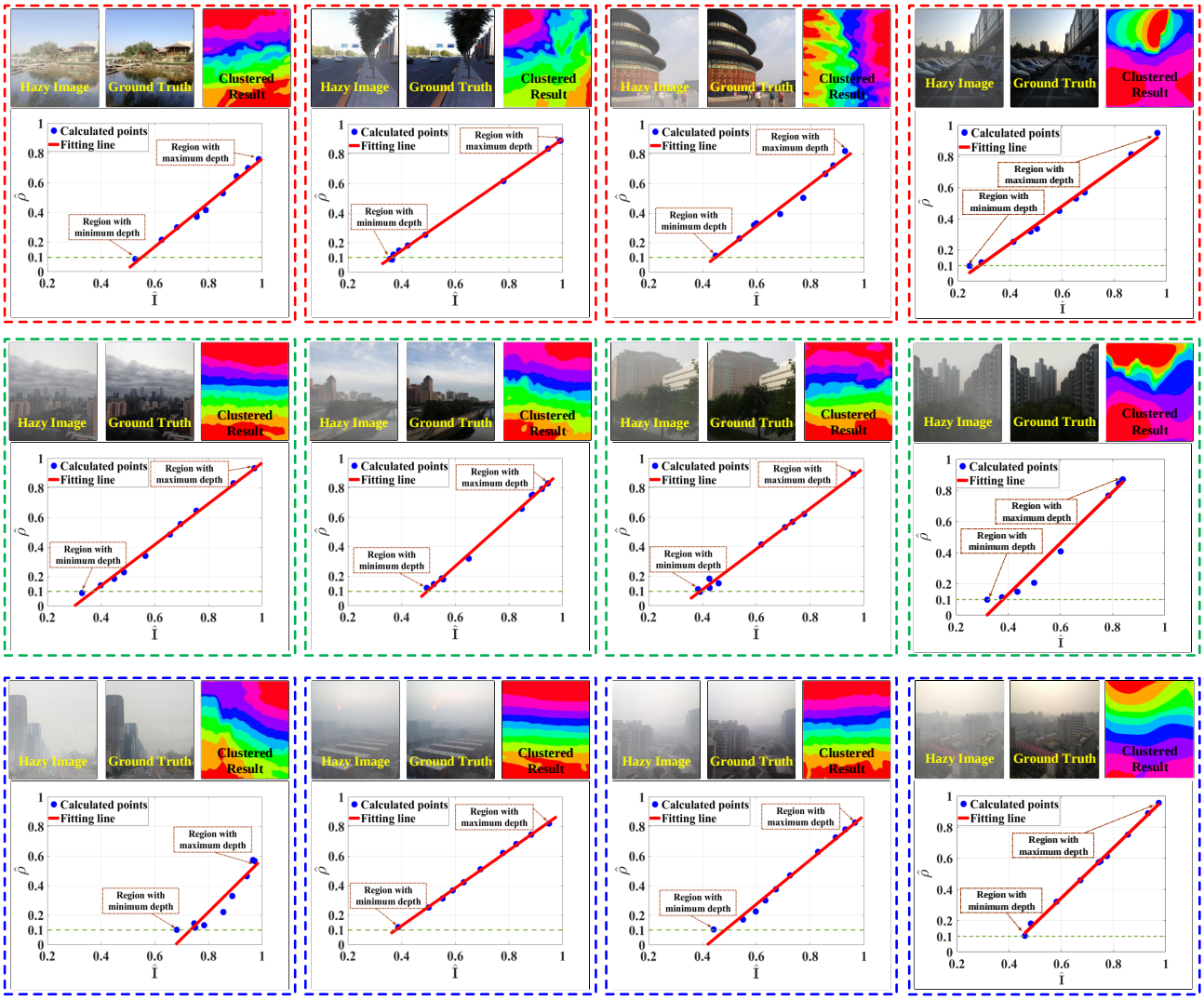

Fig. 4. Illustration of the quasi-linear relationship between $\hat{\rho}$ and $\hat{I}$ on twelve sample images. (All the images are divided into 10 regions with each region having similar scene depth).

where $(x, y) \in \Omega_m$. Since $\hat{I}_m$ and $\hat{I}_0$ are related to $\boldsymbol{I}$ and can be easily obtained via Eq. (3) once $\boldsymbol{I}$ is given, we can express RF for the m^{th} region as a function of three parameters and rewrite Eq. (8) into

$$\rho(x, y) = \mathrm{R}_m(k, \boldsymbol{A}, \boldsymbol{I}), \tag{9}$$

where $\mathrm{R_m}(\cdot)$ is the abbreviation of RF of the m^{th} region, $\boldsymbol{I}$ is the input image, only the slope k and atmospheric light $\boldsymbol{A}$ are still undetermined. Once all the regions are recovered, the entire image is re-sorted. According to Eq. (9), the derived RF successfully transforms the complex dehazing task into an estimation problem of two parameters, which significantly reduces the uncertainty of haze removal. In the next subsection, we will devise a robust and easy-to-implement method of acquiring the unknown parameters.

B. Joint Optimization

To determine the optimized values of k and $\boldsymbol{A}$, a joint optimization with two constrains is used. The essence of image dehazing is to exclude the brightness interference caused by atmospheric light during the imaging procedure. The first constraint is based on the fact that the average brightness of a high-quality image tends to have a specific value μ [58]. That is to say, we need to find a combination of k and $\boldsymbol{A}$ to minimise

$$\mathrm{F}_1(k, \boldsymbol{A}) = \left| \frac{1}{n} \cdot \sum_{m=0}^{n-1} \Psi\left[\mathrm{R_m}\left(k, \boldsymbol{A}, \boldsymbol{I}\right)\right] - \mu \right|, \tag{10}$$

where $\Psi(\cdot)$ is the mean operator. However, only utilizing this constraint to adjust the brightness is insufficient as it may cause significant information loss, i.e., some pixels will become completely black or white. Therefore, the second constraint is to guarantee a minimal loss of information when adjusting the brightness. In other words, we have to find the values of k and $\boldsymbol{A}$ to minimise

$$\mathrm{F}_2(k, \boldsymbol{A}) = \frac{1}{n} \cdot \sum_{m=0}^{n-1} \Phi\left[\mathrm{R_m}\left(k, \boldsymbol{A}, \boldsymbol{I}\right)\right], \tag{11}$$

where $\Phi(\cdot)$ is the operator to compute the information loss ratio (ILR). Considering these two constraints, a joint estima-

tion strategy is designed to seek the optimal combination of k and $\boldsymbol{A}$, i.e., k_p and $\boldsymbol{A}_p$. Formally, it can be expressed by

$$[k_p, \boldsymbol{A}_p] = \arg\min_{k,\boldsymbol{A}} \left\{ \mathrm{F}_1(k, \boldsymbol{A}) + \mathrm{F}_2(k, \boldsymbol{A}) \right\}. \tag{12}$$

Note that there are three components of the atmospheric light, i.e., $\boldsymbol{A} = \left[A^{\mathrm{R}}, A^{\mathrm{G}}, A^{\mathrm{B}}\right]$, which substantially increases the calculation overhead. To lower the complexity, a more concise form is used to define the atmospheric light:

$$\boldsymbol{A} = \tau \cdot \mathbf{o} = \tau \cdot \left[\mathrm{o}^{\mathrm{R}}, \mathrm{o}^{\mathrm{G}}, \mathrm{o}^{\mathrm{B}}\right], \tag{13}$$

where τ is the amplitude of the atmospheric light and its color direction $\mathbf{o} = \left[\mathrm{o}^{\mathrm{R}}, \mathrm{o}^{\mathrm{G}}, \mathrm{o}^{\mathrm{B}}\right]$ can be acquired by the white point method [59]. Substituting Eq. (13) into Eqs. (9)$\sim$(12), a 2-D joint optimization function (2D-JOF) in terms of k and τ is obtained as

$$[k_p, \tau_p] = \arg\min_{k,\tau} \left\{ \mathrm{F}_1(k,\tau) + \mathrm{F}_2(k,\tau) \right\} = \arg\min_{k,\tau} \left\{ \mathrm{F}(k,\tau) \right\}, \tag{14}$$

where

$$\mathrm{F}_1(k,\tau) = \left| \frac{1}{n} \cdot \sum_{m=0}^{n-1} \Psi\left[\mathrm{R}_{\mathrm{m}}\left(k, \tau \cdot \mathbf{o}, \left(\boldsymbol{I}\right)^{\downarrow_\omega}\right)\right] - \mu \right| \tag{15}$$

and

$$\mathrm{F}_2(k,\tau) = \frac{1}{n} \cdot \sum_{m=0}^{n-1} \Phi\left[\mathrm{R}_{\mathrm{m}}\left(k, \tau \cdot \mathbf{o}, \left(\boldsymbol{I}\right)^{\downarrow_\omega}\right)\right]. \tag{16}$$

Note that $\downarrow_\omega$ is a down-sampling operator with coefficient ω, which is introduced to further reduce the computational complexity. In this work, the value of ω is initialized according to [55]. It important to note that the down-sampling operation does not affect the estimation accuracy of the parameters because a down-sampled image $\left(\boldsymbol{I}\right)^{\downarrow_\omega}$ still maintains its original nature.

To solve this 2D-JOF, coordinate descent [60], [61] is a proposed candidate, in which the key idea is to alternatively minimize k and τ (by fixing the other parameter) until they converge. Specifically, the solutions of 2D-JOF after the j^{th} iteration can be computed by

$$\tau_j = \arg\min_{\tau} \left\{ \mathrm{F}(k_j, \tau) \right\}, \tag{17}$$

$$k_{j+1} = \arg\min_{k} \left\{ \mathrm{F}(k, \tau_j) \right\}, \tag{18}$$

where both Eqs. (17) and (18) are 1-D searchable problems and can be easily solved via the Fibonacci algorithm (FA). In this work, we initialize $k_1 = 0.5$ and set the stop criterion as $\delta(j) = |\tau_j - \tau_{j-1}| + |k_j - k_{j-1}| \leq \epsilon = 10^{-3}$. When the iteration is finished, the atmospheric light and the slope can be obtained as $\boldsymbol{A}_p = \tau_j \cdot \left[\mathrm{o}^{\mathrm{R}}, \mathrm{o}^{\mathrm{G}}, \mathrm{o}^{\mathrm{B}}\right]$ and $k_p = k_j$, respectively.

C. Scene Restoration

Once the slope k_p and the atmospheric light $\boldsymbol{A}_p$ are determined, the haze-free image can be easily restored by traversing all the regions using RF (Eq. (8)). However, one might observe some undesirable effects in the recovered results, which is primarily caused by the fact that the RS is implemented on the blue channel rather than using the real scene depth. To account for this deficiency, a guided filter (GF) [53] with a blurring ability is introduced, which leads to the final RF:

$$\boldsymbol{\rho}(x,y) = 1 - \mathrm{CR}(t_r) \cdot \frac{\boldsymbol{A}_p - \boldsymbol{I}(x,y)}{\boldsymbol{A}_p}, \tag{19}$$

where t_r is a rough transmission map obtained by resorting the transmission obtained by Eq. (7) for all clustered regions, and $\mathrm{CR}(\cdot)$ is the GF operator. Here we remark that one can also use other blur operators or tools to remove such interference depending on the main concerns. Fig. 5 illustrates the performance enhancement after using GF. As shown in the figure, the dehazed results obtained by Eq. (8) are evidently different to the ground truth and the color carries an unnatural appearance. In contrast, when GF is used, the obtained results look exactly the same as the ground truth.

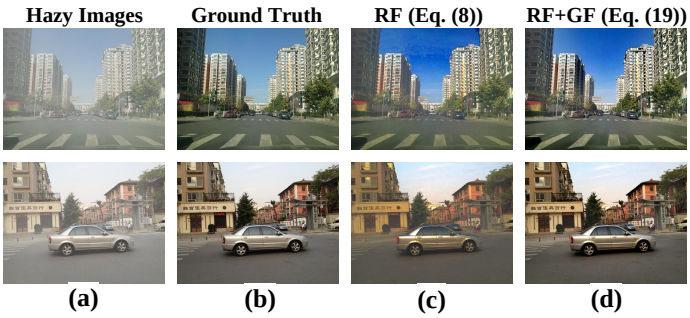

Fig. 5. Performance comparison of RF without and with GF.

For clarity, the entire procedure of the proposed IDRLP is outlined in Algorithm 1. It should be noted that all the steps are simple operations except for the iteration (steps 4 to 8). Although the iteration is relatively more complicated, Eqs. (17) and (18) can be accelerated by the down-sampling operator and are easily solved by the FA. Therefore, a high efficiency can be guaranteed.

Algorithm 1 Proposed IDRLP

Input: Hazy Image $\boldsymbol{I}$.
Pre-set parameters:
Average intensity $\mu = 0.45$, Iteration error $\epsilon = 10^{-3}$;
Initial slope $k_1 = 0.5$.
Begin

1. Region segmentation on blue channel by K-means.
2. Calculate $\hat{I}_m$ and $\hat{I}_0$ via Eq. (3).
3. Estimate color direction $\mathbf{o}$ by [59].
4. **While** $j \leq 2 \mid \delta(j) \leq \epsilon$ **do**
5. Update τ_j via Eq. (17).
6. Update k_{j+1} via Eq. (18).
7. $j = j + 1$.
8. **End While**
9. Obtain the atmospheric light via Eq. (13).
10. Restore the haze-free result $\boldsymbol{\rho}$ via Eq. (19).

End Begin
Output: Enhanced Result $\boldsymbol{\rho}$.

D. The Difference between IDRLP and IDE Proposed in [25]

Here we remark that both the IDRLP in this work and the method proposed in Ref. [25], i.e., IDE, are inspired by the phenomenon that farther regions with greater scene depth have a higher average value of pixels. However, they are intrinsically different and the two methods target at different image enhancement tasks. IDE is trying to fix an issue caused by this phenomenon (the dim effect in the dehazed result), while IDRLP takes advantage of this phenomenon to build a relationship between hazy image and its haze-free correspondence. The flowcharts illustrating the working mechanisms of the IDE and IDRLP are shown in Figs. 6(a) and 6(b), respectively.

As shown in Fig. 6(a), based on the observation, IDE introduces a light absorption rate into ASM, leading to an enhanced ASM (EASM). Then the key is to derive a transmission calculation formula (TCF) by imposing the patch-based gray world assumption (PGWA) and the atmospheric light estimated by DCP [19] on the EASM. To solve this TCF, a global stretch strategy is designed by pre-setting an acceptable saturation for enhanced results, which generates an accurate transmission map. With this transmission and the estimated atmospheric light, the haze-free result can be restored from hazy image via EASM.

According to Fig. 6(b), the first step of IDRLP is to implement region segmentation (RS) using K-means. Then, based on the proposed RLP (it utilizes the aforementioned observation to directly correlates hazy and haze-free images), the dehazing task can be transformed into a simple recovery formula (RF) composed of two unknown parameters (slope in RLP and atmospheric light). By imposing two constraints on this RF, these parameters can be solved by iteration, thereby restoring the haze-free result.

IDE aims to achieve dehazing and exposure at the same time to highlight as many details as possible, while IDRLP focuses on high-quality dehazing to ensure that the recovery result is close to the real haze-free scene. As seen in Fig. 6(a), color cast may appear in the result of IDE if DCP [19] used in it fails to utilize the haze-related feature to accurately locate atmospheric light. Compared to IDE, IDRLP exhibits a stronger robustness to deal with such complex hazy images. This advantage is due to the fact that the correlation between the parameters in IDRLP are fully utilized in Eqs. (17) and (18), which significantly increases the estimation accuracy of the atmospheric light and the slope in RF. In Section IV, we will further compare IDE in [25] and the proposed IDRLP in this paper on different kinds of images.

IV. Performance Evaluation

In this section, the performance of the proposed IDRLP is evaluated from different perspectives. First, a parameter study was conducted to determine the value of μ, which has a strong effect on the performance. Then, the atmospheric light estimated by IDRLP was evaluated and compared to that obtained by DCP [19], BCCR [22], ARAT [62], and IPR [**?**] technologies. Subsequently, we tested the proposed IDRLP on various challenging hazy images, and quantitatively and qualitatively

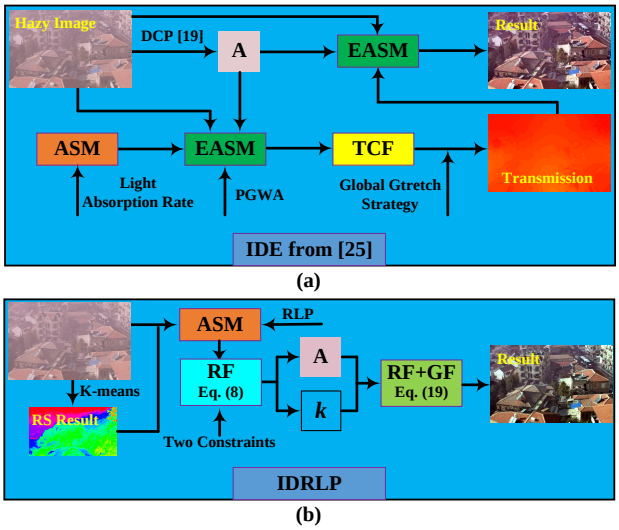

Fig. 6. The flowcharts of IDE [25] and the proposed IDRLP.

compared the results with those obtained from the state-of-art technologies, including DEFADE (TIP2015, Fusion-based) [9], NLD (TPAMI2020, Non-local-wise) [48], IDE (TIP2021, Patch-wise) [25], MSCNN (ECCV2016, Learning-wise) [32], ProxNet (ECCV2018, Learning-wise) [34], EPDN (CVPR2019, Learning-wise) [40], and MSBDN (CVPR2020, Learning-wise) [39].

A. Parameter Study

In the proposed IDRLP, as listed in Algorithm 1, there are three parameters that need to be initialized. They are the iteration error ϵ, the initial slope k_1, and the pre-set average intensity μ. Among them, the value of ϵ determines the iteration accuracy and setting $\epsilon = 10^{-3}$ is more than enough. The value of k_1 can be set to any value from interval [0 1] as its effect on the final results is negligible. It is found that the value of μ has a substantial effect on the performance. To investigate the relationship between μ and the restoration quality, a performance analysis of IDRLP using different values of μ was performed on three benchmark datasets, i.e., SOTS [52], I-HAZE [63], and O-HAZE [64]. Note that all the three datasets consist of both synthesized hazy images and their haze-free ground truth. Fig. 7(a) illustrates the results of four examples. As can be observed, the images are over-dehazed when μ is too small and the haze cover cannot be effectively removed when μ is too large.

Moreover, we calculated the peak signal-to-noise ratio (P-SNR) and structural similarity (SSIM) [65] scores of all the images in the datasets dehazed by IDRLP with different μ. Note that PSNR is used to measure the difference between the restored image and the ground truth, and SSIM has the ability to investigate the structure preservation capability. In general, larger PSNR and SSIM scores indicate a better noise immunity and a stronger structure preservation, respectively. The average PNSR and SSIM scores of the three datasets are plotted in Fig. 7(b). As can be seen, both the PNSR and SSIM scores of all the three datasets have the best results when $\mu \approx 0.45$. It should be pointed out that $\mu = 0.45$ may not be

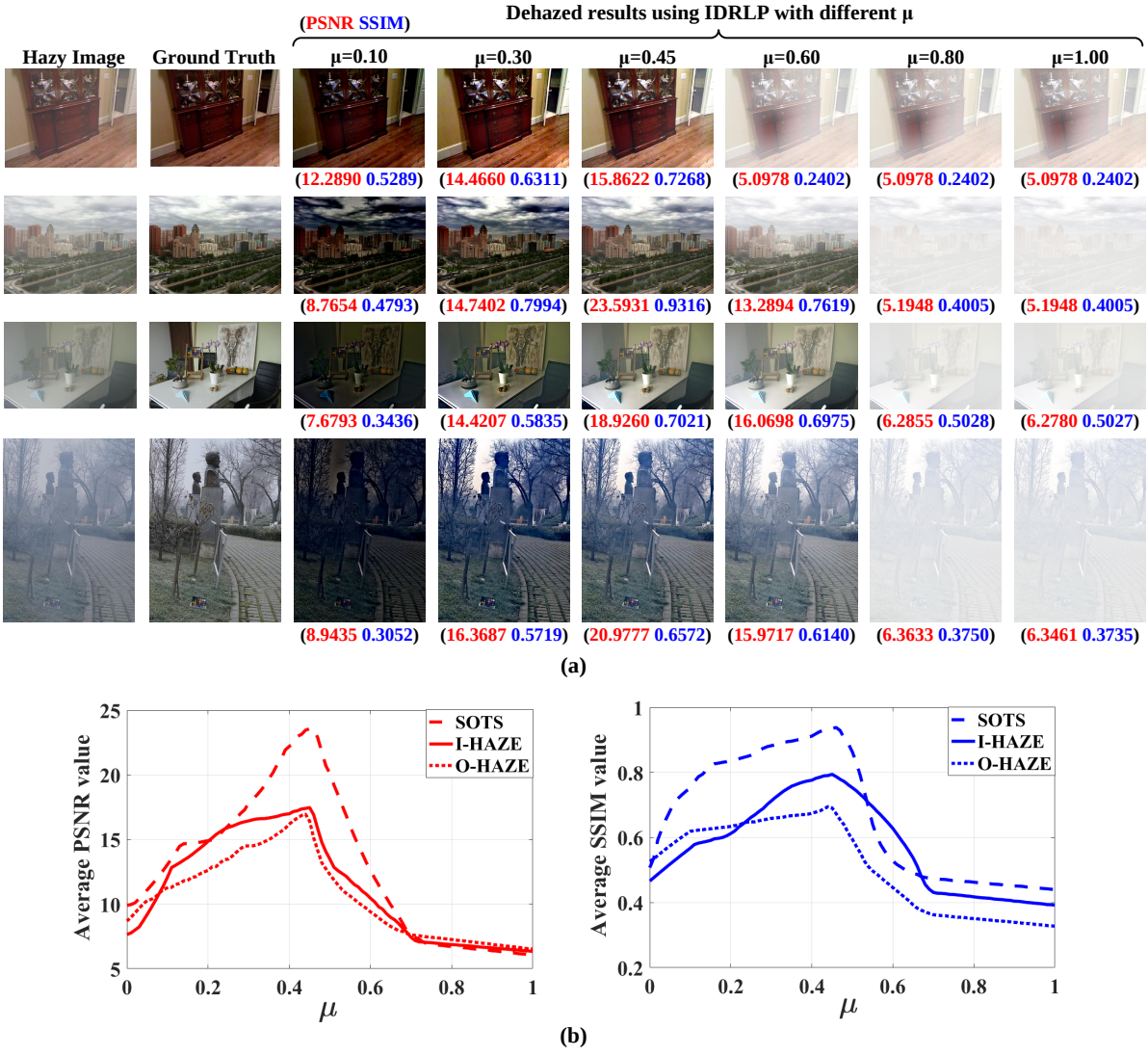

Fig. 7. (**a**): Image dehazing using the proposed IDRLP with different values of μ on four example images. (**b**): Average PNSR and SSIM scores of all the images from SOTS, I-HAZE, and O-HAZE datasets dehazed by IDRLP with different μ.

the best value for all input images, while it is indeed a pretty robust empirical parameter that can be used on all types of hazy images straightforwardly. Therefore, μ was selected to be 0.45 in this work.

B. Accuracy of Atmospheric Light

As mentioned in the introduction, most currently available ASM-based dehazing methods need to estimate the atmospheric light, which is the key step of the dehazing procedure. Despite the importance of atmospheric light estimation, it has been a challenge for these existing methods to guarantee a high degree of accuracy of the estimation across different types of images. For example, in [19], [22], [23], one needs to find the sky region and utilize the characteristics of haze to locate the atmospheric light. However, these methods will lose utility when the sky is not visible or there is some interference that influences these characteristics in the hazy image. In comparison with other works, IDRLP is based on a joint optimization strategy to search the atmospheric light, which effectively improves the estimation accuracy by making use of an entire image instead of an individual pixel.

To demonstrate the superiority of IDRLP over other techniques in locating the atmospheric light, we compared the predicted atmospheric light using IDRLP with that using DCP [19], BCCR [22], ARAT [62], and IPR [**?**] on a diverse set of 40 images compiled in [**?**]. Note that the ground truth of the atmospheric light (GToAL) was remarked for these 40 images to assure reliability. Fig. 8(a) illustrates the comparison results on three examples. It can be easily seen that for the given examples, the atmospheric light estimated by IDRLP exhibits the highest accuracy (the results are very close to the GToAL). Moreover, we further calculated the mean squared error (MSE) between the estimated atmospheric results using different methods and the GToAL of all 40 images from [**?**]. The results are illustrated in Fig. 8(b). As expected, IDRLP displays an overwhelming advantage over other techniques as it achieves the smallest average, median, and variance values of the calculated MSEs.

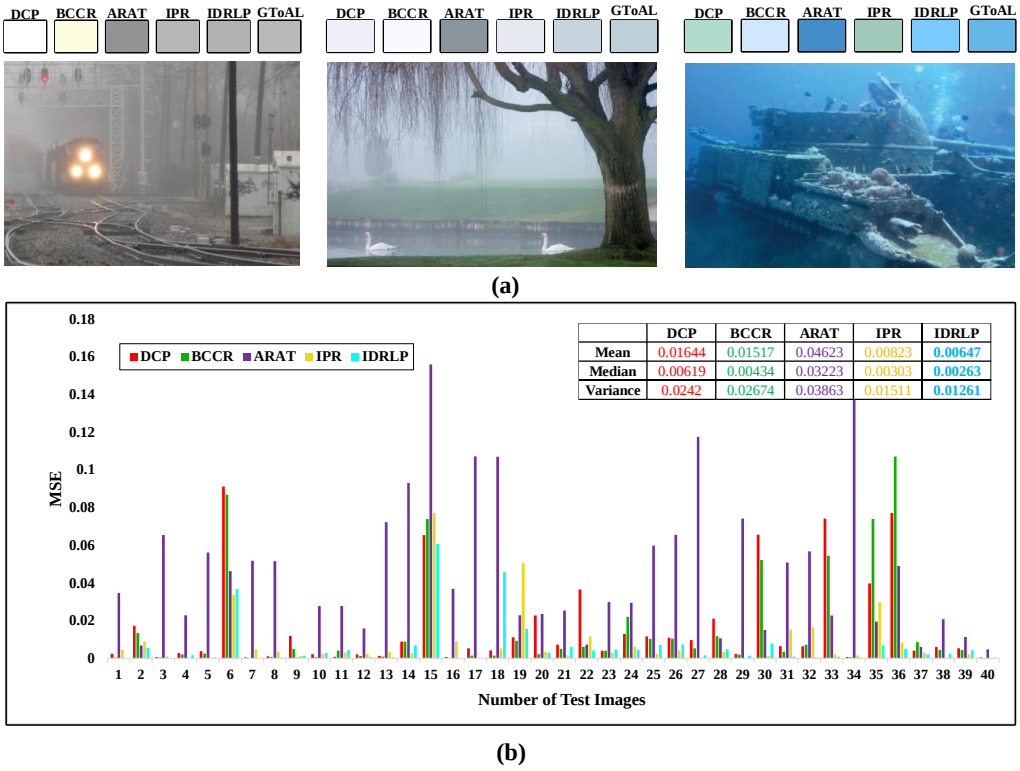

Fig. 8. Evaluating the accuracy of the estimated atmospheric light on natural images. **(a)**: Examples of hazy images, along with their manually extracted GToAL, and the estimated atmospheric light using DCP, BCCR, ARAL, IPR and IDRLP. **(b)**: Mean squared errors (MSE) between GToAL and atmospheric light calculated by different methods on 40 hazy images.

Fig. 9. Performance evaluation of IDRLP on different types of hazy images.

C. Evaluation of IDRLP

Being able to process different types of hazy images is a prerequisite for an excellent restoration algorithm. Therefore, we selected several challenging sample images from the real world to check the robustness of IDRLP. Fig. 9 shows the selected hazy images together with the dehazed results and the transmission maps attained by IDRLP. As shown in the figure, the proposed IDRLP can effectively resolve the real colors and thoroughly reveal necessary details, while the calculated transmissions are quite consistent with the human visual intuition. Most importantly, IDRLP is free from over-enhancement, over-saturation, and haze residue interferences that degrade the user experience. As displayed in these given examples, the bright scenes (e.g., sky regions and the clouds) in the dehazed images appear natural, and the necessary features covered by haze are well-enhanced. It is necessary to point out that the proposed IDRLP is able to produce a satisfactory haze-free result even when the scene depths in the image are almost a constant, see the last two examples in Fig. 9. In such case, although region segmentation (RS) errors might be introduced during implementing K-means, two key parameters (slope and atmospheric light) can still be accurately estimated by Eqs. (17) and (18) as they are calculated according to information of whole image instead of that of local patch or region. Besides, the guided filter employed in Eq. (19) can also suppress the negative visual effect caused by such RS errors.

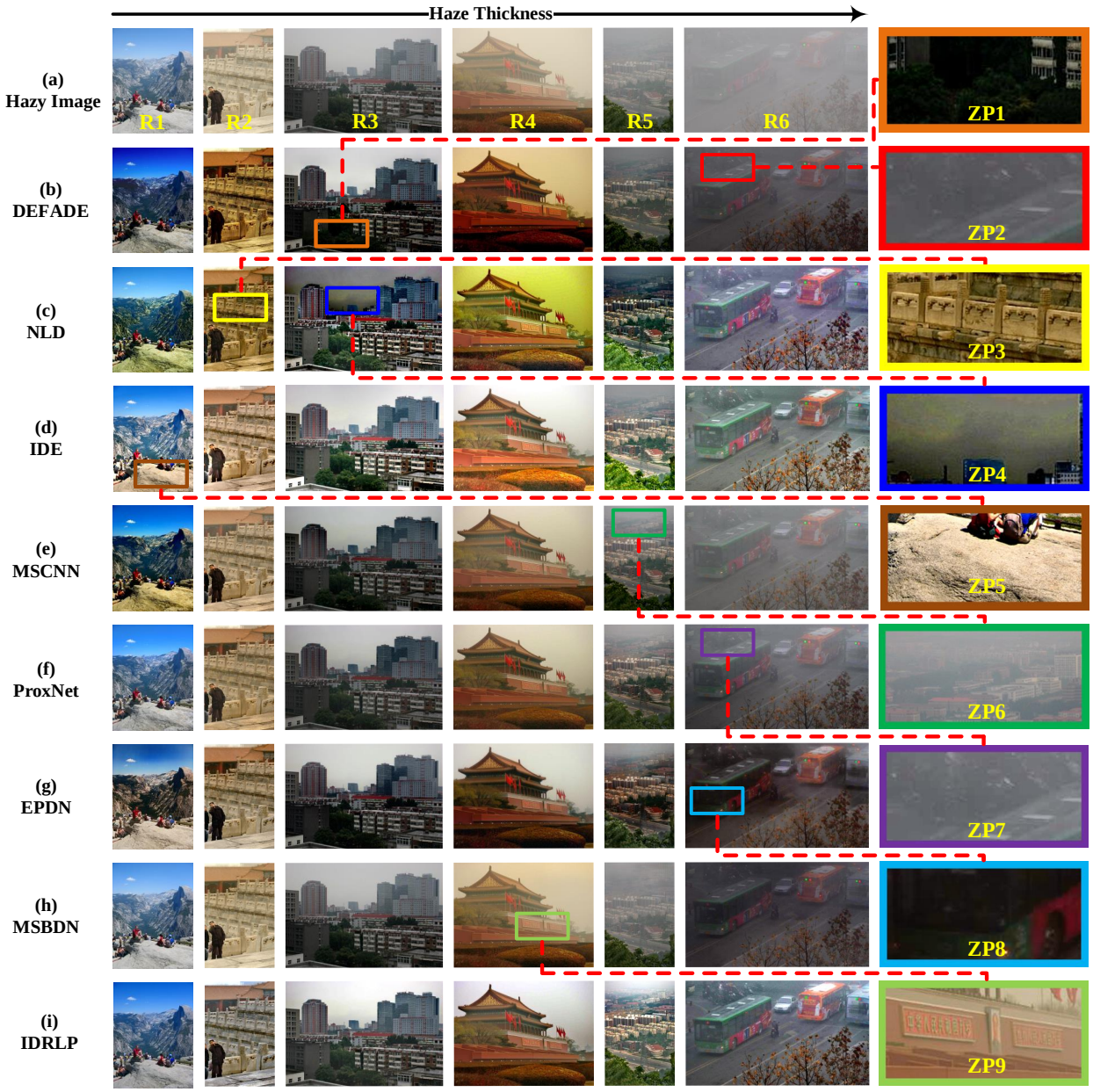

Fig. 10. Qualitative comparison of the state-of-the-art techniques on real world images.

D. Qualitative Comparison

1) Comparison on Real-World Hazy Images: To illustrate the superiority of the proposed IDRLP, we compared it against seven state-of-the-art and representative techniques, including DEFADE [9], NLD [48], IDE [25], MSCNN [32], ProxNet [34], EPDN [40], and MSBDN [39], on a variety of challenging real-world images with different haze thicknesses collected from Ref. [24]. The comparison results are illustrated in Fig. 10.

As seen in Fig. 10(b), DEFADE can identify the haze distribution and enhance the visibility for the given examples. However, it fails to deal with the images with heavy haze, and the recovered results of the misty images tend to be too dark at the surface (see the highlighted zoom-in patches ZP1 and ZP2). In Fig. 10(c), although NLD is capable of restoring the scenes and objects obscured by the haze, it suffers from over-enhancement in the sky region (ZP4) and attains over-saturated colors for the examples featuring a lot of gray (ZP3). As shown in Fig. 10(d), IDE is able to remove the haze cover and expose the potential details for given examples, but color cast is visible in the rocky region (ZP5). By observing the results in Figs. 10(e) and 10(f), both MSCNN and ProxNet are able to uncover the hidden textures and contours for the first four examples, whereas their performance deteriorates when the haze thickness becomes heavier (see ZP6 and ZP7). For EPDN as shown in Fig. 10(g), it has the ability to thoroughly eliminate the haze cover no matter what the haze thickness of the given example is. However, the results obtained by EPDN appear to be darker than they should be, e.g., the bus in ZP8. In Fig. 10(h), MSBDN can avoid some negative effects such

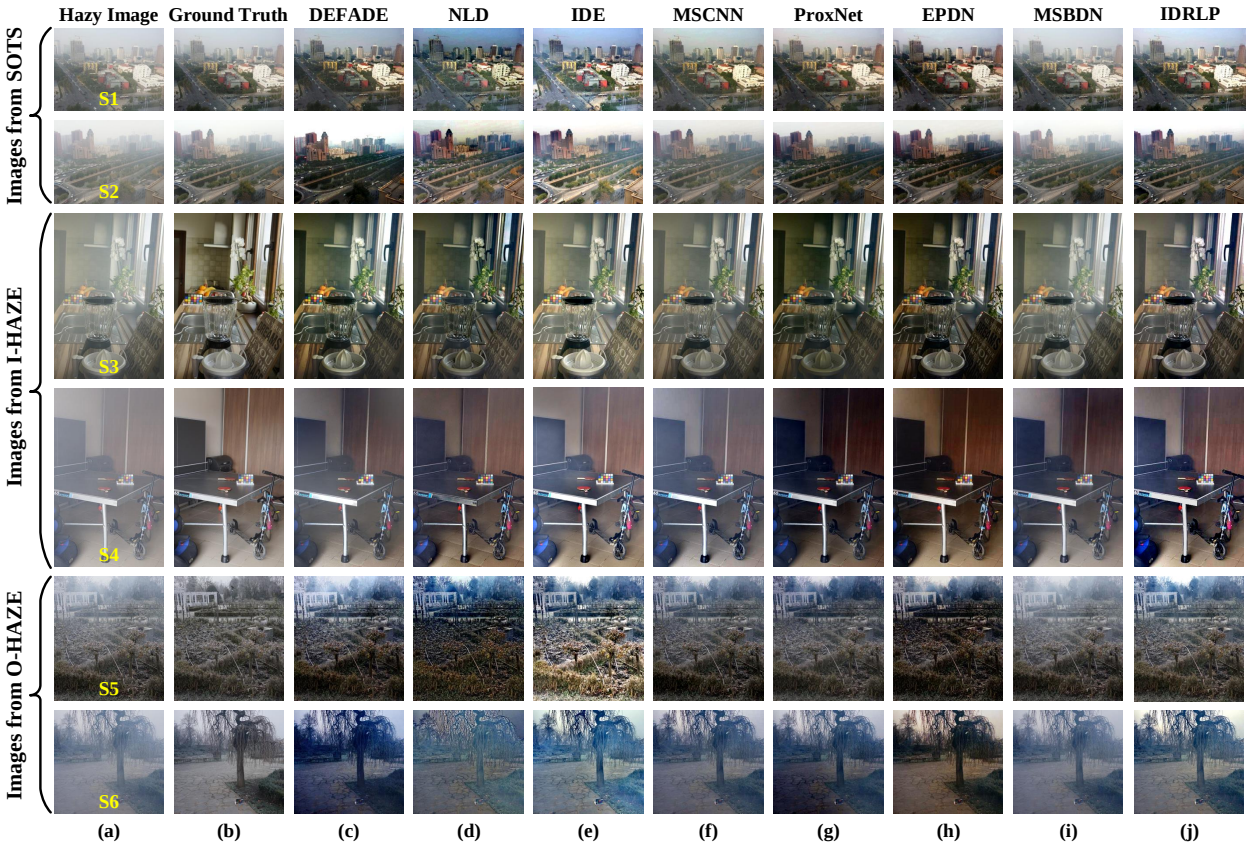

Fig. 11. Qualitative comparison between the proposed IDRLP and state-of-the-art techniques on six synthesis images.

as over-enhancement of the sky regions and color distortion of misty scenes. However, it generally has a poor performance on images with dense haze (see ZP9). In comparison, the IDRLP proposed in this work, for which the results are displayed in Fig. 10(i), achieves outstanding results. It can highlight the clear edges and restore the real colors. As observed from these recovered results, the gray-white rocks and the sky regions can be better reconstructed by IDRLP and the enhanced results look more natural and realistic than other approaches.

2) Qualitative Comparison on Synthetic Images: As mentioned in [28], it is hard to evaluate the restoration performance among different algorithms without a haze-free reference. Therefore, we further compared the proposed IDRLP with comparable state-of-the-art methods on SOTS, O-HAZE, and I-HAZE datasets that consist of both hazy images and their ground truth references. Without losing generality, six examples were chosen to conduct the comparison. The results are illustrated in Fig. 11.

In general, the comparison results are similar to those for the real-world images described in the previous subsection. As shown in Fig. 11(c), DEFADE is capable of highlighting the edges and contours for all the given examples, but the restored results appear darker than the ground truth images. In Fig. 11(d), the results obtained by NLD have rich textures and clarity. However, color distortion and over-enhancement are observed in some recovered images. According to Fig. 11(e), the haze cover and the shadow in the images can be thoroughly removed by IDE, while the color of the enhanced results of example S5 seems to be too saturated. Figs. 11(f) and 11(i) show that both MSCNN and MSBDN exhibit effective performances for most examples, but there is still a noticeable degree of haze evident in the bright areas, e.g., the wall in example S3 and the ground in example S6. Although high-quality results can be obtained by ProxNet and EPDN as shown in Figs. 11(g) and 11(h), their results appear darker than the corresponding ground truth references, which leads to visual inconsistency. In contrast, the proposed IDRLP is able to remove the haze effectively and the restored results are very close to the ground truth images for all the examples (see Figs. 11(b) and 11(j)), indicating a high degree of robustness.

E. Quantitative Comparison

To reach a more complete evaluation, the calculated PSNR and SSIM for the six images shown in Fig. 11 are summarized in Table I. It is evident from this table that IDRLP has the best scores of SSIM and PSNR for the last four examples, which indicates that the outputs of IDRLP are more similar to the ground truth compared to those of other state-of-the-art methods. For the first two examples, although IDRLP only has the second-best PSNR and SSIM values, the actual results of IDRLP are qualitatively much clearer than those of MSBDN which achieves the highest scores and even the corresponding ground truth references.

Moreover, the evaluation was further conducted with a much larger sample size. Table II lists the average PSNR and SSIM values of the dehazed results using different methods on all

TABLE I
CALCULATED PSNR AND SSIM VALUES OF THE DEHAZED RESULTS USING IDRLP AND STATE-OF-THE-ART TECHNIQUES ON THE SIX IMAGES SHOWN IN FIG. 11. (DATA IN BOLD MEANS THE BEST AND DATA IN RED INDICATES THE SECOND-BEST.)

Metric	Image	DEFADE [9]	NLD [48]	IDE [25]	MSCNN [32]	ProxNet [34]	EPDN [40]	MSBDN [39]	IDRLP
PSNR	S1	18.0934	15.5077	16.3094	16.8744	20.1954	19.4554	**31.1525**	23.9166
	S2	24.7166	15.4555	15.9776	18.3954	18.1939	18.2712	**28.3496**	24.6631
	S3	18.0567	15.7747	18.2169	18.2825	17.3509	14.9668	16.9563	**20.0093**
	S4	20.0381	15.0614	18.7158	17.3144	15.5291	13.8245	21.4035	**21.8769**
	S5	17.1711	16.8367	14.4937	20.7825	22.2129	17.0468	18.5818	**22.7703**
	S6	15.0914	16.1412	17.2408	16.9906	14.3009	16.2403	21.0918	**21.4311**
SSIM	S1	0.8561	0.6704	0.7481	0.7192	0.8552	0.8324	**0.9485**	0.9306
	S2	0.8954	0.6374	0.7055	0.8599	0.8654	0.8005	**0.9349**	0.9246
	S3	0.6988	0.7117	0.6864	0.7279	0.7401	0.6628	0.6978	**0.7597**
	S4	0.6711	0.7211	0.6714	0.4239	0.4136	0.6576	0.6776	**0.7421**
	S5	0.6398	0.6379	0.6364	0.7569	0.8189	0.6786	0.7957	**0.8606**
	S6	0.5838	0.7072	0.6158	0.6507	0.6001	0.5684	0.6826	**0.7563**

TABLE II
CALCULATED AVERAGE PSNR AND SSIM VALUES OF THE DEHAZED RESULTS USING IDRLP AND STATE-OF-THE-ART TECHNIQUES ON I-HAZE, O-HAZE, AND SOTS DATASETS. (DATA IN BOLD MEANS BEST AND DATA IN RED INDICATES THE SECOND-BEST.)

Database	Metric	DEFADE [9]	NLD [48]	IDE [25]	MSCNN [32]	ProxNet [34]	EPDN [40]	MSBDN [39]	IDRLP
I-HAZE	PSNR	15.9535	14.5387	15.9172	16.5441	14.2560	15.4013	16.699	**17.355**
	SSIM	0.7500	0.7197	0.7204	0.7783	0.7114	0.7192	0.7658	**0.7896**
O-HAZE	PSNR	15.3412	13.3776	14.2990	16.6224	16.1587	16.8574	16.4633	**16.9492**
	SSIM	0.6039	0.6094	0.6325	0.6917	0.6582	0.6793	0.6596	**0.6990**
SOTS	PSNR	16.9045	18.5907	19.2062	16.9549	20.7005	22.9536	**33.666**	23.568
	SSIM	0.7498	0.8080	0.7985	0.7592	0.8458	0.7785	**0.9876**	0.9383

TABLE III
CALCULATED PROCESSING TIME (SECONDS) OF DIFFERENT DEHAZING TECHNIQUES ON THE FIRST FOUR EXAMPLES IN FIG. 10 WITH DIFFERENT RESOLUTIONS. (DATA IN BOLD MEANS THE SHORTEST PROCESSING TIME.)

Image	Resolution	DEFADE [9] Matlab (CPU)	NLD [48] Matlab (CPU)	IDE [25] Matlab (CPU)	MSCNN [32] Matlab (CPU)	ProxNet [34] Matlab (CPU)	EPDN [40] Pytorch (CPU/GPU)	MSBDN [39] Pytorch (CPU/GPU)	IDRLP Matlab (CPU)
R1	384×256	4.6329	0.3469	0.2688	0.5463	0.9948	1.1713/0.9329	1.2926/0.2448	**0.2236**
	768×512	15.1255	1.1053	0.4263	2.2241	1.9373	1.8007/1.1131	4.7321/0.4448	**0.3710**
	1536×1024	61.6518	4.4785	1.1508	8.2105	6.5916	4.2879/1.7100	18.1626/1.2097	**0.8961**
	2304×1536	163.5108	10.2591	2.3662	17.9908	12.9918	8.7772/3.0749	40.4204/2.6119	**1.7923**
	3072×2048	559.9355	19.0473	3.9435	34.6651	25.5768	17.7368/4.9513	72.2998/—	**2.8310**
	3840×2560	—	33.2637	5.8695	90.6309	39.2949	47.2435/7.0067	112.2309/—	**3.9000**
	4608×3072	—	57.7944	8.4727	206.4190	84.6179	63.8665/12.3614	167.1191/—	**5.7305**
R2	200×300	2.5092	0.2579	0.2248	0.3243	0.8137	1.1299/0.9638	0.7490/0.2004	**0.1451**
	400×600	8.8374	0.6739	0.3484	1.3773	1.3792	1.4705/1.0228	2.6342/0.3321	**0.2140**
	800×1200	35.2334	2.4448	0.8235	4.7191	3.4135	3.1147/1.5045	9.9256/0.9720	**0.5195**
	1200×1800	90.0360	5.5109	1.5774	10.0857	6.7086	5.7403/2.3402	22.9646/2.0259	**0.9633**
	1600×2400	193.4217	10.3289	2.6529	19.1907	11.9600	9.6121/3.5019	42.1790/3.2931	**1.5216**
	2000×3000	526.5829	16.6927	3.9094	32.8263	18.0075	14.9175/5.0843	65.6165/—	**2.2902**
	2400×3600	—	27.4001	5.3295	81.2978	26.7281	33.8060/6.7136	93.8091/—	**3.2611**
R3	300×200	2.6510	0.2406	0.2502	0.3322	0.8665	1.1479/0.9308	0.6960/0.1934	**0.1504**
	600×400	8.7630	0.6230	0.3516	1.2124	1.3329	1.5465/1.0750	2.6840/0.3559	**0.2206**
	1200×800	35.7391	2.4185	0.7764	4.3774	3.1446	2.9682/1.4781	10.2122/0.9100	**0.5188**
	1800×1200	90.0897	5.3842	1.5378	9.4960	6.4491	5.6248/2.2185	23.6761/1.7473	**0.9069**
	2400×1600	208.5686	9.9252	2.5362	18.4079	11.3481	9.3365/3.2394	41.9415/2.8769	**1.5689**
	3000×2000	530.3279	16.1275	3.7725	32.3711	17.5248	14.4812/4.5555	65.7886/—	**2.3535**
	3600×2400	—	26.4553	5.1334	82.8085	25.9558	34.0248/6.0548	94.9250/—	**3.2204**
R4	300×225	2.9130	0.2635	0.2554	0.3433	0.9318	1.1872/0.9390	0.8544/0.2144	**0.1625**
	600×450	10.0109	0.6838	0.3547	1.2981	1.5903	1.5857/1.0641	2.9939/0.3727	**0.2584**
	1200×900	43.1763	2.6631	0.8545	4.7528	4.1895	3.2911/1.5713	11.5650/0.9544	**0.5496**
	1800×1350	119.5967	5.8451	1.6408	10.5000	8.6642	6.4546/2.4704	26.8620/1.9026	**0.9969**
	2400×1800	236.5677	11.6924	2.7070	19.2239	14.8764	10.4873/3.4665	47.7061/3.1996	**1.6409**
	3000×2250	750.8358	18.5929	4.2433	42.4540	23.8864	17.3574/4.9715	75.7184/—	**2.5623**
	3600×2700	—	31.5513	5.7240	132.9783	34.5697	44.6102/6.8000	103.3466/—	**3.5414**

the images in the SOTS, O-HAZE, and I-HAZE datasets. As shown in the table, IDRLP achieves the best scores for the O-HAZE and I-HAZE datasets, and the second-best results for the SOTS dataset. It's worth mentioning that MSBDN, which achieves the best average scores for the SOTS dataset, utilizes the learning-based strategy. Therefore, it may only work well on synthesized hazy images and lack the ability to generalize to the processing of real-world hazy images (see Fig. 10(h)).

F. Processing time

In addition to the recovery quality, computational efficiency is the other critical performance index for dehazing methods. As discussed at the end of Section III-C, the main overhead consumed in Algorithm 1 is the iteration, i.e., steps 4 to 8.

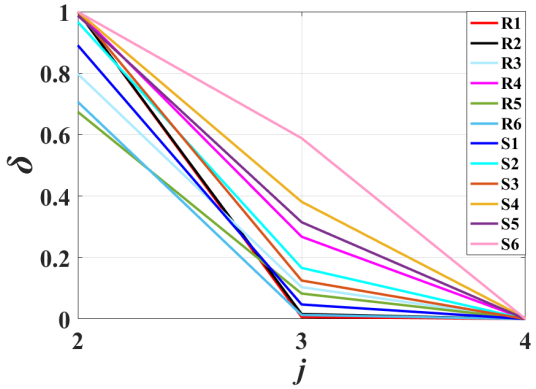

Fig. 12. Iteration curves of joint optimization module in IDRLP proposed in this work.

Given an image with resolution of $h_1 \times h_2$, the theoretical complexity of IDRLP is only $o(\frac{h_1 \times h_2}{w})$. It would be more intuitive to see how many iterations are needed for different hazy inputs to converge. Therefore, Fig. 12 plots the iteration curves for the twelve example images shown in Figs. 10 and 11, where the abscissa and ordinate are the iteration number j and the stop criterion δ, respectively. It is observed that for all the examples, only 4 iterations are needed to achieve convergence.

Furthermore, the running time for the proposed IDRLP and state-of-the-art techniques to process the first four examples in Fig. 10 with different resolutions are compared in Table III. Note that all the methods were tested on the same PC [Intel(R) Core (Tm) i7-9700k CPU@3.60GHz 16G RAM and GeForce RTX 2060 GPU] for five times without GPU acceleration and their average time costs are used. The learning-wise based EPDN and MSBDN were also tested on this PC with GPU acceleration. As shown in Table III, there is no doubt that IDRLP exhibits a much faster processing speed than the other techniques with or without GPU acceleration. In addition, this advantage becomes more pronounced when the image resolution is higher, which makes IDRLP an excellent candidate for real-time systems.

V. Conclusion

In this paper, we proposed a novel non-local region-based image prior (RLP) and used this prior to develop a single image dehazing technique, i.e., IDRLP. The proposed IDRLP translates the intricate image dehazing problem into a simple 2-D joint optimization function (2D-JOF), thereby significantly simplifying the dehazing process and reducing the processing time. Another benefit of using 2D-JOF dehazing is that it can simultaneously determine the atmospheric light and the slope used to compute transmission from the whole input image, which can leverage the correlation between parameters to improve the estimation accuracy. Experiments on a diverse set of real-world images and several widely used datasets illustrate that the proposed IDRLP is superior over state-of-the-art methods in terms of both the recovery quality and the efficiency.

References

[1] N. Hautiere, J. Tarel, and D. Aubert, "Towards fog-free in-vehicle vision systems through contrast restoration," in *2007 IEEE Conference on Computer Vision and Pattern Recognition*, 2007, pp. 1–8.

[2] A. Galdran, A. Alvarez-Gila, A. Bria, J. Vazquez-Corral, and M. Bertalmio, "On the duality between retinex and image dehazing," in *Proceedings of the IEEE Conference on Computer Vision and Pattern Recognition (CVPR)*, June 2018.

[3] J. John and M. Wilscy, "Enhancement of weather degraded video sequences using wavelet fusion," in *2008 7th IEEE International Conference on Cybernetic Intelligent Systems*, 2008, pp. 1–6.

[4] H. Xu, G. Zhai, X. Wu, and X. Yang, "Generalized equalization model for image enhancement," *IEEE Transactions on Multimedia*, vol. 16, no. 1, pp. 68–82, 2014.

[5] W. Cai, Y. Liu, M. Li, L. Cheng, and C. Zhang, "A self-adaptive homomorphic filter method for removing thin cloud," in *2011 19th International Conference on Geoinformatics*, 2011, pp. 1–4.

[6] Z. Xu, X. Liu, and X. Chen, "Fog removal from video sequences using contrast limited adaptive histogram equalization," in *2009 International Conference on Computational Intelligence and Software Engineering*, 2009, pp. 1–4.

[7] C. O. Ancuti, C. Ancuti, and P. Bekaert, "Effective single image dehazing by fusion," in *2010 IEEE International Conference on Image Processing*, 2010, pp. 3541–3544.

[8] C. O. Ancuti and C. Ancuti, "Single image dehazing by multi-scale fusion," *IEEE Transactions on Image Processing*, vol. 22, no. 8, pp. 3271–3282, 2013.

[9] L. K. Choi, J. You, and A. C. Bovik, "Referenceless prediction of perceptual fog density and perceptual image defogging," *IEEE Transactions on Image Processing*, vol. 24, no. 11, pp. 3888–3901, 2015.

[10] A. Galdran, J. Vazquez-Corral, D. Pardo, and M. Bertalmio, "Fusion-based variational image dehazing," *IEEE Signal Processing Letters*, vol. 24, no. 2, pp. 151–155, 2017.

[11] A. Galdran, "Image dehazing by artificial multiple-exposure image fusion," *Signal Processing*, vol. 149, pp. 135 – 147, 2018. [Online]. Available: http://www.sciencedirect.com/science/article/pii/S0165168418301063

[12] S. G. Narasimhan and S. K. Nayar, "Contrast restoration of weather degraded images," *IEEE Transactions on Pattern Analysis and Machine Intelligence*, vol. 25, no. 6, pp. 713–724, 2003.

[13] W. Wang, X. Yuan, X. Wu, and Y. Liu, "Fast image dehazing method based on linear transformation," *IEEE Transactions on Multimedia*, vol. 19, no. 6, pp. 1142–1155, 2017.

[14] J. Tarel and N. HautiÃĺre, "Fast visibility restoration from a single color or gray level image," in *2009 IEEE 12th International Conference on Computer Vision*, 2009, pp. 2201–2208.

[15] S. C. Raikwar and S. Tapaswi, "Lower bound on transmission using non-linear bounding function in single image dehazing," *IEEE Transactions on Image Processing*, vol. 29, pp. 4832–4847, 2020.

[16] Y. Gao, H. Hu, B. Li, Q. Guo, and S. Pu, "Detail preserved single image dehazing algorithm based on airlight refinement," *IEEE Transactions on Multimedia*, vol. 21, no. 2, pp. 351–362, 2019.

[17] Q. Liu, X. Gao, L. He, and W. Lu, "Single image dehazing with depth-aware non-local total variation regularization," *IEEE Transactions on Image Processing*, vol. 27, no. 10, pp. 5178–5191, 2018.

[18] Q. Wu, J. Zhang, W. Ren, W. Zuo, and X. Cao, "Accurate transmission estimation for removing haze and noise from a single image," *IEEE Transactions on Image Processing*, vol. 29, pp. 2583–2597, 2020.

[19] K. He, J. Sun, and X. Tang, "Single image haze removal using dark channel prior," *IEEE Transactions on Pattern Analysis and Machine Intelligence*, vol. 33, no. 12, pp. 2341–2353, 2011.

[20] T. M. Bui and W. Kim, "Single image dehazing using color ellipsoid prior," *IEEE Transactions on Image Processing*, vol. 27, no. 2, pp. 999–1009, 2018.

[21] L. He, J. Zhao, N. Zheng, and D. Bi, "Haze removal using the difference-structure-preservation prior," *IEEE Transactions on Image Processing*, vol. 26, no. 3, pp. 1063–1075, 2017.

[22] G. Meng, Y. Wang, J. Duan, S. Xiang, and C. Pan, "Efficient image dehazing with boundary constraint and contextual regularization," in *Proceedings of the IEEE International Conference on Computer Vision (ICCV)*, December 2013.

[23] J.-H. Kim, W.-D. Jang, J.-Y. Sim, and C.-S. Kim, "Optimized contrast enhancement for real-time image and video dehazing," *Journal of Visual Communication and Image Representation*, vol. 24, no. 3, pp. 410 – 425, 2013. [Online]. Available: http://www.sciencedirect.com/science/article/pii/S1047320313000242

[24] R. Fattal, "Dehazing using color-lines," *ACM Trans. Graph.*, vol. 34, no. 1, Dec. 2015. [Online]. Available: https://doi.org/10.1145/2651362
[25] M. Ju, C. Ding, W. Ren, Y. Yang, D. Zhang, and Y. J. Guo, "Ide: Image dehazing and exposure using an enhanced atmospheric scattering model," *IEEE Transactions on Image Processing*, vol. 30, pp. 2180–2192, 2021.
[26] W. Ren, J. Zhang, X. Xu, L. Ma, X. Cao, G. Meng, and W. Liu, "Deep video dehazing with semantic segmentation," *IEEE Transactions on Image Processing*, vol. 28, no. 4, pp. 1895–1908, 2019.
[27] H. Yuan, C. Liu, Z. Guo, and Z. Sun, "A region-wised medium transmission based image dehazing method," *IEEE Access*, vol. 5, pp. 1735–1742, 2017.
[28] B. Cai, X. Xu, K. Jia, C. Qing, and D. Tao, "Dehazenet: An end-to-end system for single image haze removal," *IEEE Transactions on Image Processing*, vol. 25, no. 11, pp. 5187–5198, 2016.
[29] A. Golts, D. Freedman, and M. Elad, "Unsupervised single image dehazing using dark channel prior loss," *IEEE Transactions on Image Processing*, vol. 29, pp. 2692–2701, 2020.
[30] Y. Pang, J. Nie, J. Xie, J. Han, and X. Li, "Bidnet: Binocular image dehazing without explicit disparity estimation," in *2020 IEEE/CVF Conference on Computer Vision and Pattern Recognition (CVPR)*, 2020, pp. 5930–5939.
[31] Y. Liu, J. Pan, J. Ren, and Z. Su, "Learning deep priors for image dehazing," in *2019 IEEE/CVF International Conference on Computer Vision (ICCV)*, 2019, pp. 2492–2500.
[32] W. Ren, S. Liu, H. Zhang, J. Pan, X. Cao, and M.-H. Yang, "Single image dehazing via multi-scale convolutional neural networks," in *Computer Vision – ECCV 2016*, B. Leibe, J. Matas, N. Sebe, and M. Welling, Eds. Cham: Springer International Publishing, 2016, pp. 154–169.
[33] B. Li, X. Peng, Z. Wang, J. Xu, and D. Feng, "Aod-net: All-in-one dehazing network," in *2017 IEEE International Conference on Computer Vision (ICCV)*, 2017, pp. 4780–4788.
[34] D. Yang and J. Sun, "Proximal dehaze-net: A prior learning-based deep network for single image dehazing," in *Proceedings of the European Conference on Computer Vision (ECCV)*, 2018, pp. 702–717.
[35] W. Chen, J. Ding, and S. Kuo, "Pms-net: Robust haze removal based on patch map for single images," in *2019 IEEE/CVF Conference on Computer Vision and Pattern Recognition (CVPR)*, 2019, pp. 11 673–11 681.
[36] Y. Li, Q. Miao, W. Ouyang, Z. Ma, H. Fang, C. Dong, and Y. Quan, "Lap-net: Level-aware progressive network for image dehazing," in *2019 IEEE/CVF International Conference on Computer Vision (ICCV)*, 2019, pp. 3275–3284.
[37] J. Pan, J. Dong, Y. Liu, J. Zhang, J. Ren, J. Tang, Y. W. Tai, and M. H. Yang, "Physics-based generative adversarial models for image restoration and beyond," *IEEE Transactions on Pattern Analysis and Machine Intelligence*, pp. 1–1, 2020.
[38] X. Zhang, R. Jiang, T. Wang, and W. Luo, "Single image dehazing via dual-path recurrent network," *IEEE Transactions on Image Processing*, vol. 30, pp. 5211–5222, 2021.
[39] H. Dong, J. Pan, L. Xiang, Z. Hu, X. Zhang, F. Wang, and M. H. Yang, "Multi-scale boosted dehazing network with dense feature fusion," in *2020 IEEE/CVF Conference on Computer Vision and Pattern Recognition (CVPR)*, 2020, pp. 2154–2164.
[40] Y. Qu, Y. Chen, J. Huang, and Y. Xie, "Enhanced pix2pix dehazing network," in *2019 IEEE/CVF Conference on Computer Vision and Pattern Recognition (CVPR)*, 2019, pp. 8152–8160.
[41] Y. Shao, L. Li, W. Ren, C. Gao, and N. Sang, "Domain adaptation for image dehazing," in *2020 IEEE/CVF Conference on Computer Vision and Pattern Recognition (CVPR)*, 2020, pp. 2805–2814.
[42] M. Hong, Y. Xie, C. Li, and Y. Qu, "Distilling image dehazing with heterogeneous task imitation," in *2020 IEEE/CVF Conference on Computer Vision and Pattern Recognition (CVPR)*, 2020, pp. 3459–3468.
[43] Z. Deng, L. Zhu, X. Hu, C. Fu, X. Xu, Q. Zhang, J. Qin, and P. Heng, "Deep multi-model fusion for single-image dehazing," in *2019 IEEE/CVF International Conference on Computer Vision (ICCV)*, 2019, pp. 2453–2462.
[44] X. Liu, Y. Ma, Z. Shi, and J. Chen, "Griddehazenet: Attention-based multi-scale network for image dehazing," in *2019 IEEE/CVF International Conference on Computer Vision (ICCV)*, 2019, pp. 7313–7322.
[45] X. Zhang, T. Wang, J. Wang, G. Tang, and L. Zhao, "Pyramid channel-based feature attention network for image dehazing," *Computer Vision and Image Understanding*, vol. 197-198, p. 103003, 2020.
[46] C. Li, C. Guo, J. Guo, P. Han, H. Fu, and R. Cong, "Pdr-net: Perception-inspired single image dehazing network with refinement," *IEEE Transactions on Multimedia*, vol. 22, no. 3, pp. 704–716, 2020.
[47] D. Berman, T. Treibitz, and S. Avidan, "Non-local image dehazing," in *2016 IEEE Conference on Computer Vision and Pattern Recognition (CVPR)*, 2016, pp. 1674–1682.
[48] D. Berman, T. Treibitz, and S. Avidan, "Single image dehazing using haze-lines," *IEEE Transactions on Pattern Analysis and Machine Intelligence*, vol. 42, no. 3, pp. 720–734, 2020.
[49] A. Kienle and F. Foschum, "250 years lambert surface: does it really exist?" *Opt. Express*, vol. 19, no. 5, pp. 3881–3889, Feb 2011.
[50] J. V. Anguita, M. Ahmad, S. Haq, J. Allam, and S. R. P. Silva, "Ultra-broadband light trapping using nanotextured decoupled graphene multilayers," *Science Advances*, vol. 2, no. 2, 2016. [Online]. Available: https://advances.sciencemag.org/content/2/2/e1501238
[51] Q. Zhu, J. Mai, and L. Shao, "A fast single image haze removal algorithm using color attenuation prior," *IEEE Transactions on Image Processing*, vol. 24, no. 11, pp. 3522–3533, 2015.
[52] B. Li, W. Ren, D. Fu, D. Tao, D. Feng, W. Zeng, and Z. Wang, "Benchmarking single-image dehazing and beyond," *IEEE Transactions on Image Processing*, vol. 28, no. 1, pp. 492–505, 2019.
[53] K. He, J. Sun, and X. Tang, "Guided image filtering," *IEEE Transactions on Pattern Analysis and Machine Intelligence*, vol. 35, no. 6, pp. 1397–1409, 2013.
[54] A. Likas, N. Vlassis, and J. J. Verbeek, "The global k-means clustering algorithm," *Pattern Recognition*, vol. 36, no. 2, pp. 451 – 461, 2003, biometrics. [Online]. Available: http://www.sciencedirect.com/science/article/pii/S0031320302000602
[55] M. Ju, C. Ding, Y. J. Guo, and D. Zhang, "Idgcp: Image dehazing based on gamma correction prior," *IEEE Transactions on Image Processing*, vol. 29, pp. 3104–3118, 2020.
[56] H. Ahn, D. Jang, and R. Park, "Single image dehazing with wavelength-dependent transmissions using inter-channel correlations of a colour image," *Electronics Letters*, vol. 51, no. 22, pp. 1786–1787, 2015.
[57] A. Cantor, "Optics of the atmosphere–scattering by molecules and particles," *IEEE Journal of Quantum Electronics*, vol. 14, no. 9, pp. 698–699, 1978.
[58] M. T. T. Nguyen, C. L. D. A. Mai, and N. M. Kwok, "Estimating image illuminant color based on gray world assumption," in *2011 4th International Congress on Image and Signal Processing*, vol. 2, 2011, pp. 989–993.
[59] M. S. Brennesholtz, "Projector color correction to target white points," Oct. 14 2003, uS Patent 6,631,992.
[60] S. J. Wright, "Coordinate descent algorithms," *Mathematical Programming*, vol. 151, no. 1, pp. 3–34, 2015.
[61] M. Ju, C. Ding, D. Zhang, and Y. J. Guo, "Bdpk: Bayesian dehazing using prior knowledge," *IEEE Transactions on Circuits and Systems for Video Technology*, vol. 29, no. 8, pp. 2349–2362, 2019.
[62] M. Sulami, I. Glatzer, R. Fattal, and M. Werman, "Automatic recovery of the atmospheric light in hazy images," in *2014 IEEE International Conference on Computational Photography (ICCP)*. IEEE, 2014, pp. 1–11.
[63] C. O. Ancuti, C. Ancuti, R. Timofte, and C. D. Vleeschouwer, "I-haze: a dehazing benchmark with real hazy and haze-free indoor images," in *arXiv:1804.05091v1*, 2018.
[64] C. O. Ancuti, C. Ancuti, R. Timofte, and C. De Vleeschouwer, "O-haze: A dehazing benchmark with real hazy and haze-free outdoor images," in *2018 IEEE/CVF Conference on Computer Vision and Pattern Recognition Workshops (CVPRW)*, 2018, pp. 867–8678.
[65] Zhou Wang, A. C. Bovik, H. R. Sheikh, and E. P. Simoncelli, "Image quality assessment: from error visibility to structural similarity," *IEEE Transactions on Image Processing*, vol. 13, no. 4, pp. 600–612, 2004.

Mingye Ju received a Bachelor degree in communication engineering from Nanjing University of Posts and Telecommunications, Nanjing, China, in 2010; a PH.D degree from Nanjing University of Posts and Telecommunications, Nanjing, China, in 2018; and a PH.D degree from Global Big Data Technologies Centre (GBDTC), University of Technology Sydney, Sydney, Australia, in 2020. He is currently a lecturer with the School of Internet of Things, Nanjing University of Posts and Telecommunication, Nanjing, China. Meanwhile, he is also a postdoctoral researcher at Nanjing University of Science and Technology. His research interests include computer vision and image processing.

Can Ding (M'16) received a Bachelor degree in Micro-electronics from Xidian University, Xi'an, China, in 2009; and a PHD degreed from Macquarie University, Sydney, Australia, in 2015. From 2012 to 2015, he is under the cotutelle agreement between Macquarie University, Australia and Xidian University, China. During this period, he is also with Commonwealth Scientific and Industrial Research Organisation (CSIRO) DPaS Flagship, Marsfield, Australia. From 2015 to 2017, he was a postdoctoral Research Fellow in University of Technology Sydney (UTS), Sydney, Australia. He is currently a lecturer with Global Big Data Technologies Centre (GBDTC), University of Technology Sydney (UTS), Sydney, Australia. He is an ARC DECRA fellow since 2020. His research interest is in the area of antennas and THz fibres.

Charles A. Guo received his Bachelor of Science from the University of Sydney in 2019. He is currently pursuing a Ph.D. degree in the School of Electrical and Telecommunications Engineering, University of New South Wales, New South Wales, Australia. He has been employed as a part-time Research Fellow at the University of Technology Sydney since 2018. Charles' current research interest includes artificial intelligence, signal and image processing, Internet of Things (IoT) and digital twin.

Wenqi Ren (M'18) Wenqi Ren received the Ph.D. degree from Tianjin University in 2017. From 2015 to 2016, he was a Joint-Training Ph.D. Student in electrical engineering and computer science with the University of California at Merced, Merced, CA, USA. He is currently an Assistant Professor with the Institute of Information Engineering, Chinese Academy of Sciences, China. His research interests include image/video analysis and enhancement, and related vision problems.

Dacheng Tao (Fellow, IEEE) is the President of the JD Explore Academy and a Senior Vice President of JD.com. He is also an advisor and chief scientist of the digital science institute in the University of Sydney. He mainly applies statistics and mathematics to artificial intelligence and data science, and his research is detailed in one monograph and over 200 publications in prestigious journals and proceedings at leading conferences. He received the 2015 Australian Scopus-Eureka Prize, the 2018 IEEE ICDM Research Contributions Award, and the 2021 IEEE Computer Society McCluskey Technical Achievement Award. He is a fellow of the Australian Academy of Science, AAAS, ACM and IEEE.